nature nanotechnology

LETTERS

https://doi.org/10.1038/s41565-019-0606-8

Regioselective magnetization in semiconducting nanorods

Tao-Tao Zhuang[1,2,10], Yi Li[1,10], Xiaoqing Gao[3,4,10], Mingyang Wei[2], F. Pelayo García de Arquer[2], Petar Todorović[2], Jie Tian[5], Gongpu Li[1], Chong Zhang[1], Xiyan Li[2], Liang Dong[1], Yonghong Song[6], Yang Lu[6], Xuekang Yang[3], Libing Zhang[7], Fengjia Fan[8], Shana O. Kelley[7,9], Shu-Hong Yu[1*], Zhiyong Tang[3*] and Edward H. Sargent[2*]

Chirality—the property of an object wherein it is distinguishable from its mirror image—is of widespread interest in chemistry and biology[1–6]. Regioselective magnetization of one-dimensional semiconductors enables anisotropic magnetism at room temperature, as well as the manipulation of spin polarization—the properties essential for spintronics and quantum computing technology[7]. To enable oriented magneto-optical functionalities, the growth of magnetic units has to be achieved at targeted locations on a parent nanorod. However, this challenge is yet to be addressed in the case of materials with a large lattice mismatch. Here, we report the regioselective magnetization of nanorods independent of lattice mismatch via buffer intermediate catalytic layers that modify interfacial energetics and promote regioselective growth of otherwise incompatible materials. Using this strategy, we combine materials with distinct lattices, chemical compositions and magnetic properties, that is, a magnetic component (Fe_3O_4) and a series of semiconducting nanorods absorbing across the ultraviolet and visible spectrum at specific locations. The resulting heteronanorods exhibit optical activity as induced by the location-specific magnetic field. The regioselective magnetization strategy presented here enables a path to designing optically active nanomaterials for chirality and spintronics.

Optical chirality is often pursued in nanomaterials and can be tuned via electric (μ) and magnetic (m) dipoles[8]. To date, the chemical construction of chiral nanomaterials has been achieved through the introduction of chiral molecules and geometrically helical structures[9] to provide modulation of μ, but this limits structural stability and electrical conductivity (Supplementary Table 1). Designing magneto-optical nanomaterials that exhibit a local magnetic field to modulate the relationship between μ and m and achieve chirality[10] shows promise, but remains an area for further work and demonstration.

One-dimensional chalcogenide nanohybrids with programmed components[11–15] are compelling candidates for chiral applications owing to their potential high circular dichroism (CD) intensity, thanks to the combination effects of size, shape and constituent elements[7].

To induce a local, oriented magnetic field in one-dimensional chalcogenide materials requires the regioselective incorporation of magnetic domains, such as Fe_3O_4 (a prototypical ferrimagnetic material showing high stability, abundance and ease of preparation)[16–18], at specific locations on one-dimensional supports; however, this has been challenging due to the large lattice and chemical mismatch between one-dimensional chalcogenide semiconductors and magnetites[19,20].

In initial trials, when using ZnS nanorods (typical ultraviolet-absorbing one-dimensional chalcogenide) as seeds, we found that Fe_3O_4 self-nucleated rather than going through heteroepitaxy on ZnS (Supplementary Fig. 1). The poor wettability of Fe_3O_4 nanocrystals on semiconducting sulfide nanorod substrates can be ascribed to their low crystalline compatibilities (Supplementary Table 2).

We sought, therefore, to control the wettability between magnetites and a series of semiconducting sulfide nanorods (that is, $Zn_xC_{1-x}S$, where $0 \leq x \leq 1$) in a way that would ultimately enable their regioselective integration.

Wettability, a major factor affecting the heterogeneous growth between the seed and overgrown material[21], can be quantified by the contact angle θ (see Supplementary Note 1 for calculation). We summarize in Fig. 1a–c the contact angles between different materials, to describe how to build up controlled wettability and regioselective epitaxy. For example, when x approaches 1, the contact angle between the Fe_3O_4 nanocrystal and the $Zn_xCd_{1-x}S$ nanorod is too large to realize the heteroepitaxy (Fig. 1a). Large values of the contact angle correspond to relatively small energy barriers between heterogeneous nucleation and homogeneous nucleation, resulting in poor wettability. The intermediate crystalline mismatch (Supplementary Table 2) between $Zn_xCd_{1-x}S$ and Au enables heterogeneous growth (Supplementary Fig. 2) with multiple nucleation sites, consistent with the cases where the contact angles fall within the range 30°–150° (Fig. 1b). The crystalline mismatch of Au-Fe_3O_4 (<3%, Supplementary Table 2) is negligible, signifying that contact angles in these systems are low enough to obtain good wettability and thus lead to the core–shell structures (Fig. 1c).

[1]Division of Nanomaterials & Chemistry, Hefei National Laboratory for Physical Sciences at Microscale, CAS Center for Excellence in Nanoscience, Institute of Biomimetic Materials & Chemistry, Department of Chemistry, University of Science and Technology of China, Hefei, China. [2]Department of Electrical and Computer Engineering, University of Toronto, Toronto, Ontario, Canada. [3]CAS Key Laboratory of Nanosystem and Hierarchical Fabrication, CAS Center for Excellence in Nanoscience, National Center for Nanoscience and Technology, Beijing, China. [4]College of Physics and Optoelectronic Engineering, Shenzhen University, Guangdong, China. [5]Engineering and Materials Science Experiment Center, University of Science and Technology of China, Hefei, China. [6]School of Biological and Medical Engineering, School of Chemistry and Chemical Engineering, Hefei University of Technology, Hefei, China. [7]Department of Pharmaceutical Sciences, Leslie Dan Faculty of Pharmacy, University of Toronto, Toronto, Ontario, Canada. [8]CAS Key Laboratory of Microscale Magnetic Resonance and Department of Modern Physics, University of Science and Technology of China, Hefei, China. [9]Department of Chemistry, University of Toronto, Toronto, Ontario, Canada. [10]These authors contributed equally: Tao-Tao Zhuang, Yi Li, Xiaoqing Gao.
*e-mail: shyu@ustc.edu.cn; zytang@nanoctr.cn; ted.sargent@utoronto.ca

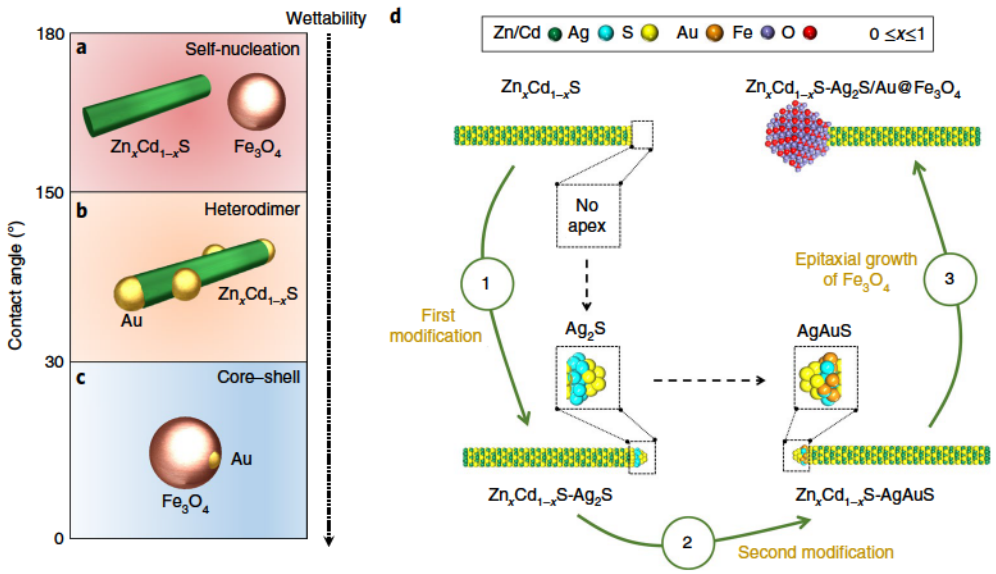

Fig. 1 | Regioselective magnetization of one-dimensional nanorods. a–c, Heterogeneous nucleation and growth as a function of the contact angle θ between two different domains. Self-nucleation between a $Zn_xCd_{1-x}S$ (for example, $x=1$, shown in Supplementary Fig. 1) nanorod and an Fe_3O_4 nanocrystal occurs when there is a large θ (>150°) corresponding to poor wetting (**a**); $Zn_xCd_{1-x}S$-Au heterodimers arise when the contact angle θ is between 150° and 30° (**b**); the formation of core–shell nanostructure (Au@Fe_3O_4) occurs with a small contact angle (<30°, good wettability) (**c**). **d**, Schematic illustration of the growth process to anchor a magnetic component at an apex of a one-dimensional nanorod, that is, a quaternary $Zn_xCd_{1-x}S$-Ag_2S/Au@Fe_3O_4 heteronanorod. Step 1: selectively modifying one apex of the $Zn_xCd_{1-x}S$ nanorod to become binary $Zn_xCd_{1-x}S$-Ag_2S; step 2: preparing $Zn_xCd_{1-x}S$-AgAuS heteronanorod from binary $Zn_xCd_{1-x}S$-Ag_2S by selectively integrating Au atoms into the Ag_2S apex; step 3: preparing a quaternary $Zn_xCd_{1-x}S$-Ag_2S/Au@Fe_3O_4 heteronanorod in the shape of a hammer from a $Zn_xCd_{1-x}S$-AgAuS heteronanorod by epitaxially growing the Fe_3O_4 nanodomain on the Au shell.

A nanorod has three positional options that can support the heterogeneous nucleation and growth of the second nanocrystal, including apex-I, side-II and apex-III (Supplementary Fig. 3). Tuning the surface activity among these three positions offers a strategy to realize heterogeneous nucleation and growth at a single location. We took the view that the targeted growth of an Fe_3O_4 nanodomain at one apex of a $Zn_xCd_{1-x}S$ nanorod could be directed by sequentially introducing intermediate catalytic materials that modify the interfacial energy locally, and thus favour site-selective nucleation.

We therefore developed a double-buffer-layer engineering strategy to achieve the site-specific nucleation of magnetite (Fe_3O_4) through the buffering layers of Ag_2S and Au. The Ag_2S tip, which catalyses the growth of $Zn_xCd_{1-x}S$ nanorods, triggers the site-selective integration of Au into the tip as a result of the lower reaction energy. The Au tip further dictates regioselective growth of the magnetic domain at one apex of each nanorod.

We first tuned bare $Zn_xCd_{1-x}S$ to possess a small Ag_2S apex at one end of the parent, one-dimensional semiconductor substrate (Fig. 1d, step 1), providing a high reaction activity site (the Ag_2S apex) among the three positions of a nanorod, for further integration of Au.

With the initial reactive site formed, we then sought to selectively integrate Au with the Ag_2S apex; Au would further function as an adhesion layer, facilitating the growth of an Fe_3O_4 nanocrystal[22,23]. We deposited Au into Ag_2S at low temperature (0 °C), leading to the sequential modification of the Ag_2S apex to form AgAuS (Fig. 1d, step 2).

Using the as-prepared $Zn_xCd_{1-x}S$-AgAuS nanorod as the seed, we further grew an Fe_3O_4 domain epitaxially at one apex (Fig. 1d, step 3), leading to the final one-dimensional $Zn_xCd_{1-x}S$-Ag_2S/Au@Fe_3O_4 quaternary heteronanorods.

Specifically, to illustrate this concept, we then synthesized Ag_2S-tipped sulfide nanorods (Fig. 2a and Supplementary Fig. 4) including ZnS-Ag_2S (Fig. 2b(i)), $Zn_{0.9}Cd_{0.1}S$-Ag_2S (Fig. 2b(ii)), $Zn_{0.5}Cd_{0.5}S$-Ag_2S (Fig. 2b(iii)), $Zn_{0.3}Cd_{0.7}S$-Ag_2S (Fig. 2b(iv)) and CdS-Ag_2S (Fig. 2b(v)) by a colloidal catalyst-assisted growth method (details in Methods). We tuned Ag_2S to AgAuS (Supplementary Fig. 5) and thereafter obtained $Zn_xCd_{1-x}S$-Ag_2S/Au@Fe_3O_4 (Fig. 2c,d) by a double-buffer-layer (Ag_2S/Au) growth strategy. Taking ZnS-Ag_2S/Au@Fe_3O_4 as an example, we optimized the reaction temperature, reductant and molar ratio of solvents (Supplementary Fig. 6 and Supplementary Note 2) to realize the nucleation and growth of an Fe_3O_4 domain at only one apex of the ZnS nanorod (Supplementary Fig. 7). The yield of this selective growth is high: almost all heteronanorods observed had Fe_3O_4 domains at one end of the structure, as assessed using transmission electron microscopy (TEM).

We tuned the absorption of these nanorods across the ultraviolet and visible regime by controlling the Zn/Cd ratio (Fig. 2e,f). The quaternary compounds fabricated herein show a broadened excitonic absorption (Fig. 2f), a consequence of the integration of Au and Fe_3O_4 domains. Powder X-ray diffraction patterns support the coexistence of these components (Fig. 2g). The peaks that belong to Fe_3O_4 are well indexed with the face-centred cubic phase (JCPDS 72-2303, cyan standard lines in Fig. 2g). The presence of Au peaks reflects the initial AgAuS apex transformed to Ag_2S/Au with a thin Au shell during the heating process (Supplementary Figs. 8 and 9). The lattice strain between Ag_2S and Fe_3O_4 caused Au to be extracted from AgAuS to form an intermediate Au layer (Supplementary Fig. 10), thus relaxing the strain.

Taking ZnS-Ag_2S/Au@Fe_3O_4 as an example, we further examined the structure and formation mechanism of the synthesized quaternary heteronanorods. High resolution high-angle annular dark-field scanning transmission electron microscopy (HR-HAADF–STEM) analysis (Fig. 3a and Supplementary Fig. 11) provides information about the detailed crystal planes and heteroepitaxial direction. Driven by the initial ZnS-Ag_2S configuration, both Au and the ensuing Fe_3O_4 grow along the $[111]_{cubic}$ crystal direction (Fig. 3b,c) owing to the good lattice match between Au(111) and Fe_3O_4(111) (Fig. 3d and Supplementary Table 2). We performed energy dispersive X-ray spectroscopy (EDS) mapping analysis and found that Zn

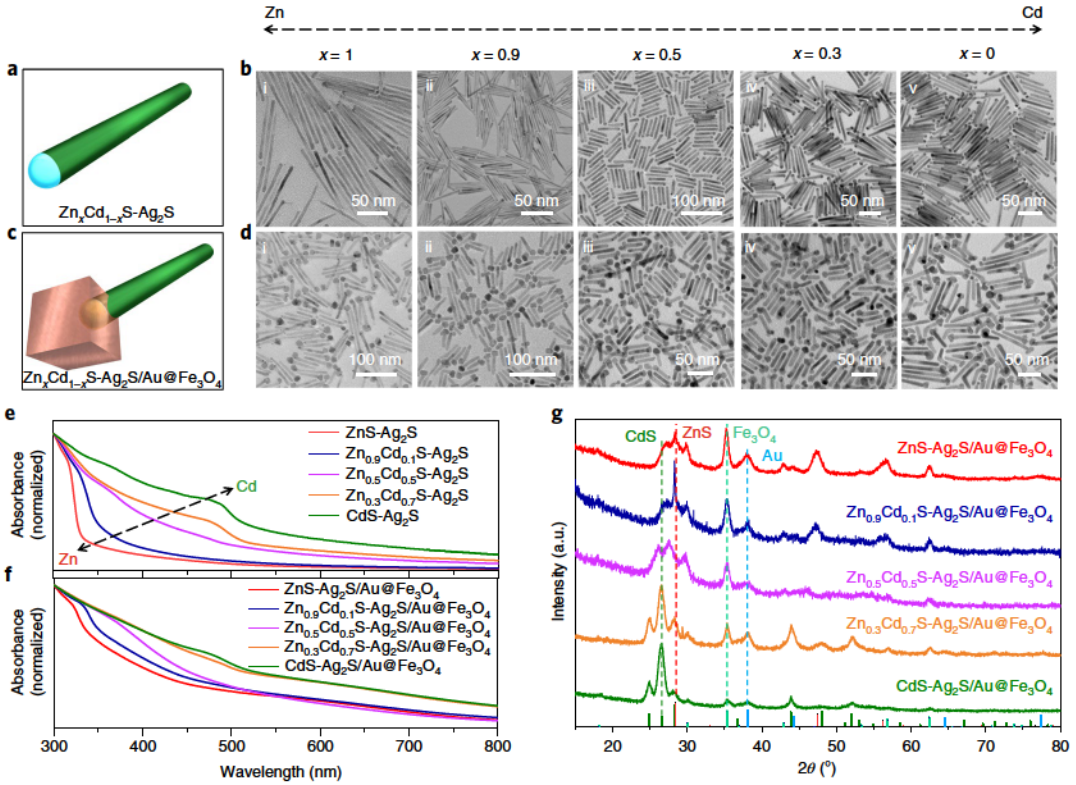

Fig. 2 | Structural characterization of $Zn_xCd_{1-x}S$-Ag_2S/Au@Fe_3O_4 heteronanorods. a, Model of $Zn_xCd_{1-x}S$-Ag_2S. **b**, TEM images of $Zn_xCd_{1-x}S$-Ag_2S nanorods. ZnS-Ag_2S ($x=1$) (**b**(i)); $Zn_{0.9}Cd_{0.1}S$-Ag_2S ($x=0.9$) (**b**(ii)); $Zn_{0.5}Cd_{0.5}S$-Ag_2S ($x=0.5$) (**b**(iii)); $Zn_{0.3}Cd_{0.7}S$-Ag_2S ($x=0.3$) (**b**(iv)); CdS-Ag_2S ($x=0$) (**b**(v)). **c**, Model of $Zn_xCd_{1-x}S$-Ag_2S/Au@Fe_3O_4. **d**, TEM images of $Zn_xCd_{1-x}S$-Ag_2S/Au@Fe_3O_4 nanorods. ZnS-Ag_2S/Au@Fe_3O_4 ($x=1$) (**d**(i)); $Zn_{0.9}Cd_{0.1}S$-Ag_2S/Au@Fe_3O_4 ($x=0.9$) (**d**(ii)); $Zn_{0.5}Cd_{0.5}S$-Ag_2S/Au@Fe_3O_4 ($x=0.5$) (**d**(iii)); $Zn_{0.3}Cd_{0.7}S$-Ag_2S/Au@Fe_3O_4 ($x=0.3$) (**d**(iv)); CdS-Ag_2S/Au@Fe_3O_4 ($x=0$) (**d**(v)). **e**, Optical absorption spectra of binary $Zn_xCd_{1-x}S$-Ag_2S with various Zn/Cd ratios, covering the absorption range from ultraviolet to visible light. **f**, Optical absorption spectra of quaternary $Zn_xCd_{1-x}S$-Ag_2S/Au@Fe_3O_4, showing the broadened excitonic absorption compared with the corresponding binary seeds. **g**, X-ray diffraction patterns, verifying the components in these quaternary heteronanorods. Standard JCPDS cards: 65-0309 for ZnS (red), 65-3414 for CdS (green), 04-0784 for Au (blue) and 72-2303 for Fe_3O_4 (cyan).

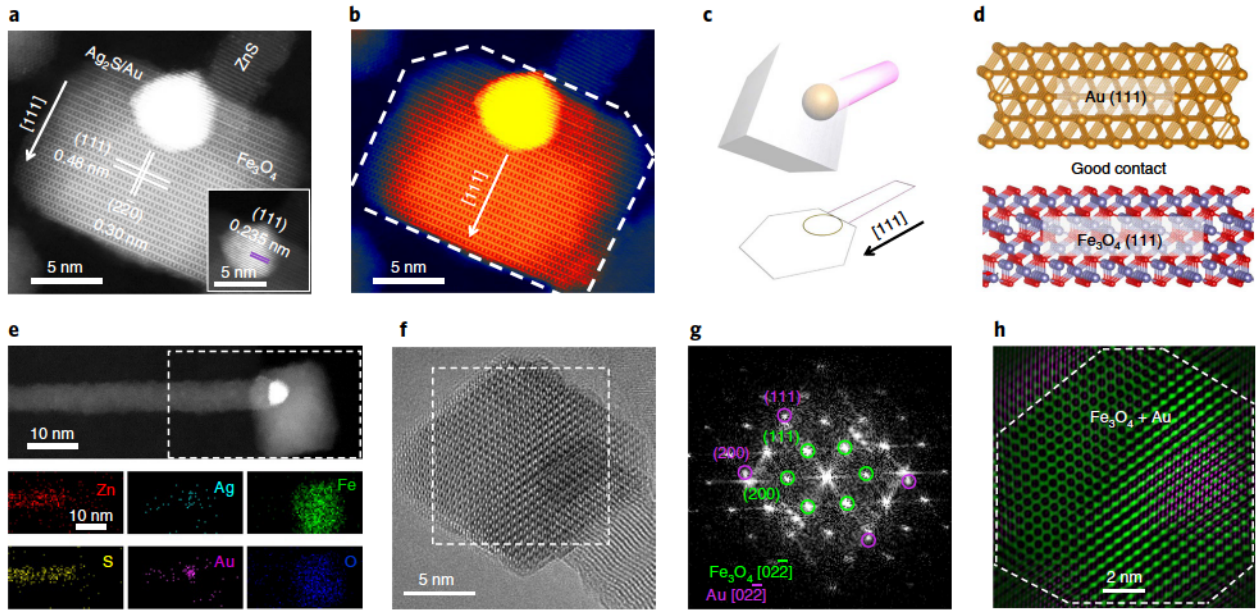

Fig. 3 | Growth of quaternary heteronanorods. a, HR-HAADF–STEM images of ZnS-Ag_2S/Au@Fe_3O_4 show the planes of each component, demonstrating the epitaxial growth direction along the [111] axis. Inset: cropped HR-HAADF–STEM image with adjusted brightness and contrast, highlighting the *d* spacing of the Au(111) planes. **b**, Pseudocolor image of **a**, showing the contrast differences for different components. **c**, 3D model of the quaternary heteronanorod and corresponding 2D projected model from top view. **d**, Atomic models of the Au(111) plane and Fe_3O_4(111) plane. **e**, EDS elemental mapping images of ZnS-Ag_2S/Au@Fe_3O_4, revealing the distribution of these four units in the nanorod. **f**, HRTEM image of a $Zn_{0.9}Cd_{0.1}S$-Ag_2S/Au@Fe_3O_4 heteronanorod apex. **g**, FFT image from the white dashed square in **f**. **h**, Superimposed colour-coded inversed FFT image from **g** with masked spots.

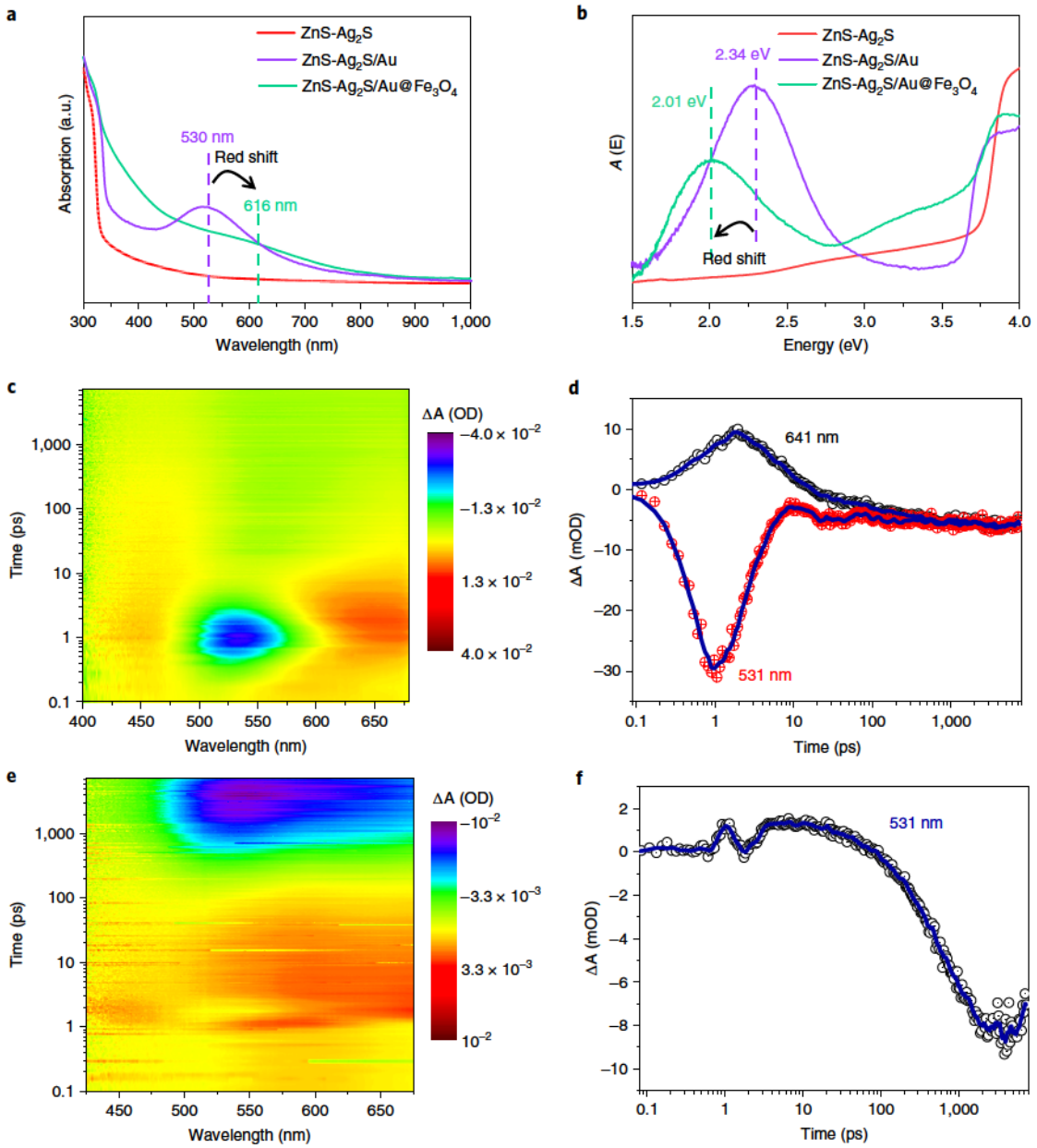

Fig. 4 | Optical absorption spectroscopy. a, The evolution of the absorption peak with component integration during the growth of quaternary ZnS-Ag_2S/Au@Fe_3O_4 heteronanorods. **b**, Jacobian transformation of the optical absorption from **a**, showing the plasmonic absorption features. **c**,**d**, Pseudocolour plot of the transient absorption spectrum (**c**) and transient signals at 531 nm and 641 nm (**d**) for ZnS-Ag_2S/Au. **e**,**f**, Pseudocolour plot of the transient absorption spectrum (**e**) and transient signals at 531 nm (**f**) for ZnS-Ag_2S/Au@Fe_3O_4. OD, optical density.

and S enrich in the stem, whereas Au, Ag and S are present in the apex and Fe and O are found to distribute in the epitaxial region (Fig. 3e and Supplementary Fig. 12). X-ray photoelectron spectroscopy analysis (Supplementary Fig. 13) further confirmed the presence of each component (ZnS, Ag_2S, Au and Fe_3O_4). We also utilized fast Fourier transforms (FFTs) of TEM images to examine another sample ($Zn_{0.9}Cd_{0.1}S$-Ag_2S/Au@Fe_3O_4), and again found a lattice-matched epitaxial relationship between Au and Fe_3O_4 in heteronanorods (Fig. 3f–h and Supplementary Fig. 14).

The compositional and structural transformations are further reflected in the optical properties of the material (Fig. 4a,b). The absorption spectrum for the ternary ZnS-Ag_2S/Au structure (purple curve) exhibits plasmonic absorption at 2.34 eV (Fig. 4b), attributed to the Au nanocrystals, which were segregated from AgAuS and went through ripening on heating. This Au surface plasmon resonance band red shifts to 2.01 eV (Fig. 4b), broadens and decays in intensity after the growth of the Fe_3O_4 component. We ascribe these changes to the increased local dielectric constant around Au domains with the encapsulation of Fe_3O_4 shells and charge transfer from Au to Fe_3O_4, thus leading to a deficient electron population in Au: the scarce population of electrons in the Au component causes the plasmonic absorption to shift to longer wavelength.

We then used transient absorption spectroscopy to investigate the electron dynamics of the nanorod heterostructures. We observed a negative absorption feature at 531 nm and a wide photon-induced absorption at 641 nm in ZnS-Ag_2S/Au samples (Fig. 4c). The negative feature (Fig. 4d) is attributed to the plasmon band bleach, with an average lifetime of 3 ps (ref. [24]). However, for the ZnS-Ag_2S/Au@Fe_3O_4, the plasmon band bleach disappeared within an initial 100 ps (Fig. 4e,f), suggesting that the Fe_3O_4 component

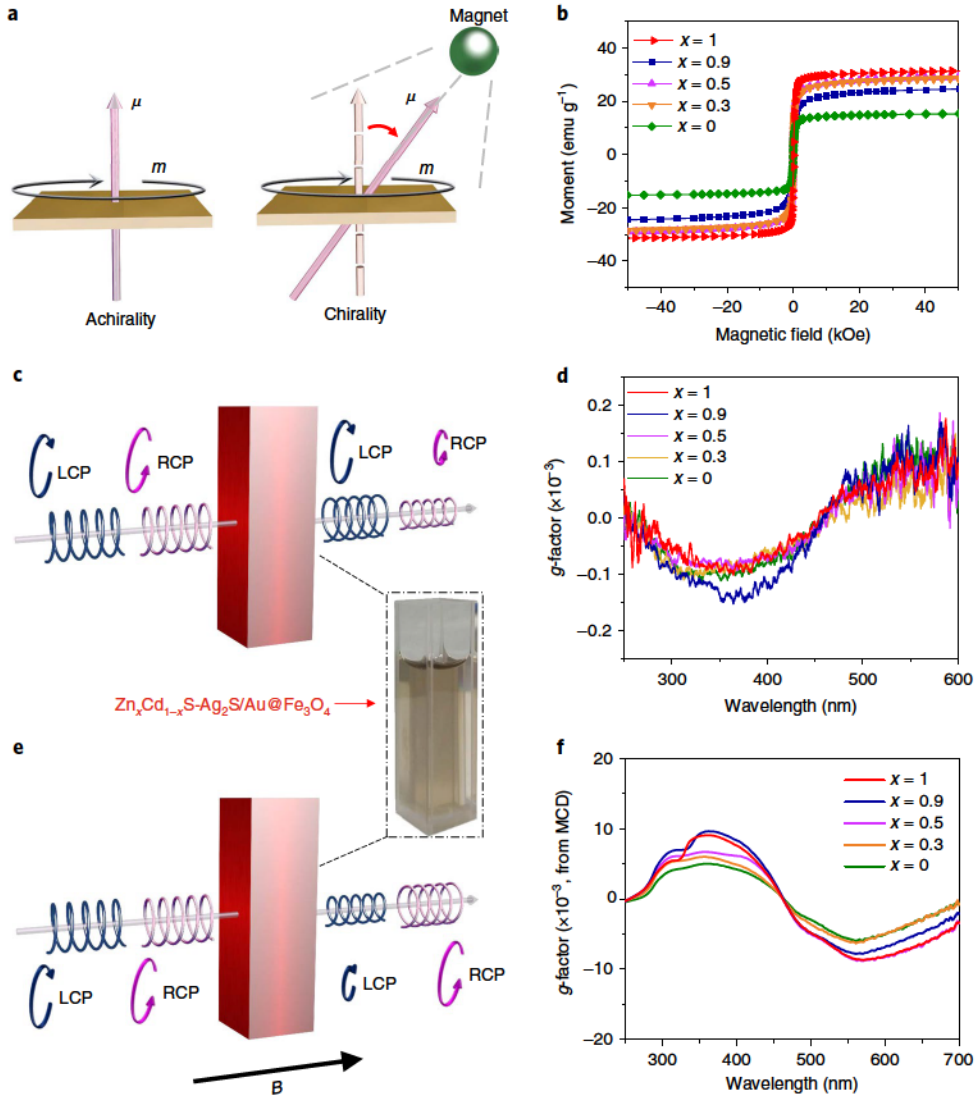

Fig. 5 | Local magnetic field induces optical activity in colloidal hybrid nanostructures. a, Materials show the achirality when the electric dipole moment μ is perpendicular to the magnetic dipole moment m in electron transition states (left panel); while the interaction of m and μ induces optical activity when a local magnetic field is applied, which causes deflection of μ (right panel). **b**, Hysteresis loop curves at 300 K, indicating the superparamagnetism in all $Zn_xCd_{1-x}S$-Ag_2S/Au@Fe_3O_4 (x=1, 0.9, 0.5, 0.3, 0) heteronanorods. **c**, Schematic of CD set-up. **d**, Anisotropic g-factor spectra of colloidal heteronanorods obtained from CD. **e**, Schematic of MCD set-up with magnetic field in parallel with the excitation light. **f**, Anisotropic g-factor spectra of colloidal heteronanorods obtained from MCD at 1.6 T. B, magnetic field.

has electronic interactions with the Au intermediate shell. The modified plasmon band, together with the modified dynamics of plasmonic hot electrons, supports the catalytic function of Au in the Fe_3O_4 growth and the existence of interfacial interactions between these two epitaxial materials.

We further analysed the structures of these quaternary heteronanorods in detail to verify the morphology and composition distributions (Supplementary Figs. 15–19 and Supplementary Table 3).

We demonstrated that the regioselective magnetization of these colloidal nanorods gives rise to chiroptical activity. The equation for chiroptical activity is written as:[25]

$$R = \mathrm{Im}(\mu \cdot m) \quad (1)$$

where R is rotational strength (the intensity of chirality), μ is the electric transition dipole moment for the transition from final state to the initial one and m is the magnetic transition dipole moment for the reverse transition.

Electronic transitions in achiral materials take the form shown in Fig. 5a (left panel) with the μ perpendicular to m. When one applies a local magnetic field, the Lorentz force of charges will deflect the direction of μ with little change of the transition energy (Fig. 5a, right panel). Hence, due to the local magnetic field, the dot product in equation (1) will no longer be zero, corresponding to the generation of chiroptical activity.

The site-specific Fe_3O_4 nanoparticle at the apex of the nanorod introduces a local magnetic field in the semiconductor nanorod and ligands around it, and magnetizes the nanorod from diamagnetism to superparamagnetism (Fig. 5b and Supplementary Fig. 20). Thus, the new hybrid materials exhibit optical activity owing to the angle deflection between μ and m induced by the magnetic field. Under excitation with left-handed circularly polarized (LCP) and right-handed circularly polarized (RCP) light, the chiroptical activity in heteronanorods causes different degrees of absorption of LCP and RCP light due to spin-dependent transition selection rules (Fig. 5c). We observed anisotropic g-factor spectra arising from CD in these

quaternary materials, while we observed no optical activity without Fe_3O_4 (Fig. 5d and Supplementary Figs. 21 and 22). The nanocompounds of $Zn_{0.9}Cd_{0.1}S$-Ag_2S/Au@Fe_3O_4 exhibit higher optical activity compared with $Zn_xCd_{1-x}S$-Ag_2S/Au@Fe_3O_4 heteronanorods of other Zn/Cd ratios.

The influence of the local magnetic field is further confirmed by the magnetic circular dichroism (MCD) (Fig. 5e). Without Fe_3O_4 nanoparticles, the semiconductor nanorods exhibit diamagnetism, with the MCD increasing linearly with the magnetic field intensity (Supplementary Fig. 23). Once we introduce Fe_3O_4, these hybrids were magnetized, with their MCD independent of the applied magnetic field intensity (Supplementary Fig. 24). Figure 5f shows the anisotropic *g*-factor spectra of $Zn_xCd_{1-x}S$-Ag_2S/Au@Fe_3O_4 at 1.6 T. The heteronanorods show the highest value when x is 0.9, a finding that we ascribe to the fact that this stoichiometry endows Zn/Cd semiconductor nanorods with the highest electric dipole moment[14]. The regioselective magnetification strategy here offers opportunities for chiral catalysis, circularly polarized photoluminescence and spintronics (Supplementary Note 3).

We further carried out magnetothermal and photothermal tests on the heteronanorods. The materials exhibit two-mode thermal responses (Supplementary Fig. 25) when magnetic field and photoirradiation are applied.

In summary, we report a double-buffer-layer engineering strategy—sequential two-step modifications of the nanorod apex with buffer layers (Ag_2S and Au)—to achieve regioselective nucleation of magnetic nanodomains (Fe_3O_4) at one end of semiconducting nanorods. These findings indicate an approach to catalytic growth that facilitates the desired nucleation site on one-dimensional nanorods. We demonstrate magnetically induced optical activity and magnetic-optical-plasmonic functions in these heteronanorods. We further anchored the magnetic oxide domain in another semiconductor system, selenide (Supplementary Fig. 26), highlighting the wider application of this method. This work provides avenues for the design and realization of heteronanostructures exhibiting controlled regioselective configurations with physical/chemical properties distinct from non-selective structures.

Online content

Any methods, additional references, Nature Research reporting summaries, source data, extended data, supplementary information, acknowledgements, peer review information; details of author contributions and competing interests; and statements of data and code availability are available at https://doi.org/10.1038/s41565-019-0606-8.

Received: 17 July 2018; Accepted: 2 December 2019;
Published online: 20 January 2020

References

1. Berova, N. & Nakanishi, K. in *Cicular Dichroism, Principles and Applications* (eds Berova, N. et al.) Ch. 8 (Wiley, 1994).
2. Rikken, G. L. J. A. & Raupach, E. Observation of magneto-chiral dichroism. *Nature* **390**, 493–494 (1997).
3. Barron, L. D. Chirality and magnetism shake hands. *Nat. Mater.* **7**, 691–692 (2008).
4. Yin, P., Tan, Y., Fang, H., Hegde, M. & Radovanovic, P. V. Plasmon-induced carrier polarization in semiconductor nanocrystals. *Nat. Nanotechnol.* **13**, 463–467 (2018).
5. Yeom, J. et al. Chiromagnetic nanoparticles and gels. *Science* **359**, 309–314 (2018).
6. Gao, X. et al. Distinct excitonic circular dichroism between wurtzite and zincblende CdSe nanoplatelets. *Nano Lett.* **18**, 6665–6671 (2018).
7. Gao, X. et al. Excitonic eircular dichroism of chiral quantum rods. *J. Am. Chem. Soc.* **139**, 8734–8739 (2017).
8. Barron, L. D. *Molecular Light Scattering and Optical Activity* (Cambridge Univ. Press, 2009).
9. Ma, W. et al. Chiral inorganic nanostructures. *Chem. Rev.* **117**, 8041–8093 (2017).
10. Gao, X., Han, B., Yang, X. & Tang, Z. Perspective of chiral colloidal semiconductor nanocrystals: opportunity and challenge. *J. Am. Chem. Soc.* **141**, 13700–13707 (2019).
11. Wu, X. J. et al. Controlled growth of high-density CdS and CdSe nanorod arrays on selective facets of two-dimensional semiconductor nanoplates. *Nat. Chem.* **8**, 470–475 (2016).
12. Oh, N. et al. Double-heterojunction nanorod light-responsive LEDs for display applications. *Science* **355**, 616–619 (2017).
13. Tan, C., Chen, J., Wu, X.-J. & Zhang, H. Epitaxial growth of hybrid nanostructures. *Nat. Rev. Mater.* **3**, 17089 (2018).
14. Zhuang, T.-T. et al. A unique ternary semiconductor–(semiconductor/metal) nano-architecture for efficient photocatalytic hydrogen evolution. *Angew. Chem. Int. Ed. Engl.* **54**, 11495–11500 (2015).
15. Li, Y. et al. Pulsed axial epitaxy of colloidal quantum dots in nanowires enables facet-selective passivation. *Nat. Commun.* **9**, 4947 (2018).
16. Laurent, S. et al. Magnetic iron oxide nanoparticles: synthesis, stabilization, vectorization, physicochemical characterizations, and biological applications. *Chem. Rev.* **108**, 2064–2110 (2008).
17. Ho, D., Sun, X. & Sun, S. Monodisperse magnetic nanoparticles for theranostic applications. *Acc. Chem. Res.* **44**, 875–882 (2011).
18. Ling, D., Lee, N. & Hyeon, T. Chemical synthesis and assembly of uniformly sized iron oxide nanoparticles for medical applications. *Acc. Chem. Res.* **48**, 1276–1285 (2015).
19. Lee, J., Yang, J., Kwon, S. G. & Hyeon, T. Nonclassical nucleation and growth of inorganic nanoparticles. *Nat. Rev. Mater.* **1**, 16034 (2016).
20. Tan, C., Chen, J., Wu, X.-J. & Zhang, H. Epitaxial growth of hybrid nanostructures. *Nat. Rev. Mater.* **3**, 17089 (2018).
21. Sun, Y. Interfaced heterogeneous nanodimers. *Nat. Sci. Rev.* **2**, 329–348 (2015).
22. Song, J. et al. Double-layered plasmonic–magnetic vesicles by self-assembly of Janus amphiphilic gold–iron(II,III) oxide nanoparticles. *Angew. Chem. Int. Ed. Engl.* **56**, 8110–8114 (2017).
23. Lou, Z. et al. Anisotropic Ag_2S–Au triangular nanoprisms with desired configuration for plasmonic photocatalytic hydrogen generation in visible/near-infrared region. *Adv. Funct. Mater.* **28**, 1706969 (2018).
24. Logunov, S. L., Ahmadi, T. S., El-Sayed, M. A., Khoury, J. T. & Whetten, R. L. Electron dynamics of passivated gold nanocrystals probed by subpicosecond transient aAbsorption. *Spectrosc. J. Phy. Chem. B* **101**, 3713–3719 (1997).
25. Rodger, A., Nordén, B. & Nordén, B. *Circular Dichroism and Linear Dichroism* (Oxford Univ. Press, 1997).

Methods

Materials. The reagents $AuCl_3$, potassium hydroxide (KOH), hexane (97%), toluene (99.5%), chloroform ($CHCl_3$), methanol (99.5%), ethanol (99.7%), 1-dodecanethiol (97%) and oleic acid (OA, 85%) were purchased from Sigma-Aldrich. 1-Hexadecanol, oleylamine (OAm, 80–90%), octadecene, mercaptopropionic acid and ferric acetylacetonate ($Fe(acac)_3$) were purchased from Aladdin Chemicals. All chemicals were used as received without further purification. $HAuCl_4$ solution was prepared by dissolving 1 g of $AuCl_3$ in 20 ml of toluene and 20 ml of OAm, forming a light yellow solution.

Catalysed growth of Ag_2S-tipped $Zn_xCd_{1-x}S$ nanorods. The $Zn_xCd_{1-x}S$ nanorods were synthesized via a catalyst-assisted method according to the previous report, with some modifications[26]. Typically, metal–diethyldithiocarbamate (dedc) precursors of $Zn(dedc)_2$ and $Cd(dedc)_2$ were mixed with Ag(dedc), 1-dodecanethiol and OA in a flask. The reaction was heated to 210 °C within 20 min and maintained for 5 min. OA (10 ml) was then injected into the hot solution. The solution temperature dropped down and quickly recovered to 210 °C. The reaction was kept at 210 °C for the growth of nanorods, and this was followed by precipitation with ethanol. The products were centrifuged and then washed twice with hexane and ethanol for further use. The detailed synthetic parameters for different nanorods are provided in Supplementary Table 4.

Integration of Au into the Ag_2S apex of $Zn_xCd_{1-x}S$ nanorods. Typically, 20 mg of $Zn_xCd_{1-x}S$ nanorods were well dispersed in 20 ml of toluene and kept at 0 °C, then 200 µl of $HAuCl_4$ solution was added to the above solution. The reaction was kept for 2 h, followed by precipitation with ethanol. The products were centrifuged and then washed twice with hexane and ethanol for further use.

Synthesis of $Zn_xCd_{1-x}S$-Ag_2S/Au@Fe_3O_4 heteronanorods. The $Zn_xCd_{1-x}S$-Ag_2S/Au@Fe_3O_4 heteronanorods were synthesized via an epitaxial growth process. Typically, 10 mg of $Zn_xCd_{1-x}S$-AgAuS nanorods were well dispersed in a solution of 5 ml of octadecene, 1 ml of OA and 1.2 ml of OAm. 1-Hexadecanol (300 mg) and 24 mg of $Fe(acac)_3$ were added into the solution and degassed at 100 °C for 30 min to remove air and water. The reaction was then switched to an Ar atmosphere and heated to 300 °C at a ramp rate of 3 °C min^{-1}. The reaction was kept at 300 °C for 1 h for the nucleation and growth of Fe_3O_4 nanodomains. The products were centrifuged and then washed twice with hexane and ethanol for further use.

Phase transfer of hydrophobic nanocrystals to aqueous solution. The hydrophobic nanocrystals were transferred from hydrophobic to hydrophilic media via a ligand exchange in two-phase solution according to previous reports[11,12]. Mercaptopropionic acid (200 µl) was added into 15 ml of chloroform with 10 mg of sample. The turbid solution was stirred for 3 h, followed by centrifugation. The precipitate was washed with acetone and further dried in a vacuum chamber. The products were centrifuged and then washed twice with ethanol for magnetothermal and photothermal tests.

Characterization. The X-ray diffraction patterns were measured on a Philips X'Pert Pro Super X-ray diffractometer equipped with graphite-monochromatized Cu Kα radiation (wavelength $\lambda = 1.5406$ Å). X-ray photoelectron spectra were determined on an X-ray photoelectron spectrometer (ESCALab MKII) with an excitation source of Mg Kα radiation (1,253.6 eV). The binding energies were referred to the C 1*s* peak (284.8 eV) from adventitious carbon. Nanocrystals dispersed in hexane were drop-casted on carbon-supported Cu grids for TEM and high-resolution TEM (HRTEM) observations, which were performed on Hitachi H-7700 and JEOL-2100F microscopes with an acceleration voltage of 100 kV and 200 kV, respectively. EDS mapping and HAADF–STEM were carried out using JEOL Arm-200F and Talos F200X electron microscopes operated at 200 kV. Ultraviolet–visible absorption spectra were collected on a UV-2600 spectrophotometer (Shimadzu) at room temperature with nanocrystals dispersed in toluene. The magnetic properties were acquired using a superconducting quantum interference device (SQID, MPMS XL5). The magnetic hyperthermia response was tested on a high-frequency (315 kHz) heating machine (Shuangping). Inductively coupled plasma–mass spectrometry (ICP-MS) was carried out on PlasmaQuad 3 to analyse the Zn, Cd and Fe content in each sample.

Transient absorption measurements. The 1,030-nm fundamental (5 kHz) was produced by a Yb:KGW regenerative amplifier (Pharos, Light Conversion). A portion of this beam was sent through an optical parametric amplifier (Orpheus, Light Conversion) to generate the 3.4-eV photoexcitation pulse (pulse duration ~250 fs). Both the photoexcitation and fundamental were sent into an optical bench (Helios, Ultrafast). The fundamental, after passing through a delay stage, was focused into a sapphire crystal, generating the probe as a white light continuum. The frequency of the photoexcitation pulse was reduced to 2.5 kHz using a chopper. Both beams were then focused onto the sample, which was housed in a 1-mm cuvette. The probe was then detected by a CCD (Helios, Ultrafast).

CD and MCD tests. CD spectra were recorded by a Jasco J-1500 spectropolarimeter in solution. A 3-ml portion of each sample was infused into a 1 × 1 cm^2 quartz cell and measured at a scan speed of 200 nm min^{-1} with a bandwidth of 4 nm. MCD spectra were also detected by the Jasco J-1500 spectropolarimeter in solution with a magnetic field of 0.4 T, 0.7 T, 1.0 T, 1.3 T and 1.6 T, respectively. Here, a 1.5-ml portion of each sample was infused into a 0.5 × 1 cm^2 quartz cell and measured at the scan speed of 200 nm min^{-1} with a bandwidth of 4 nm.

Calculation of anisotropic *g*-factor from CD and ultraviolet–visible absorption spectra. CD involving LCP and RCP light is an important means to characterize the optically active materials. When circularly polarized light passes through an absorbing optically active medium, the absorbed extent between LCP and RCP light differs ($\varepsilon_L \neq \varepsilon_R$). The CD is the difference $\Delta\varepsilon = \varepsilon_L - \varepsilon_R$ (ref. [25]). Here, the vertical coordinate of the CD spectrum is ellipticity θ (mdeg), which is

$$\theta = 3.3 \times 10^4 \times \Delta\varepsilon \times C \times l \quad (2)$$

where C is the solute concentration and l is the path length. As for chiral nanocrystals, anisotropic *g*-factor is a key parameter to determine the optical activity due to its ready availability by comparing the CD spectrum with the absorption spectrum. The equation is as follows:[27,28]

$$g = \frac{\theta}{3.3 \times 10^4 \times A} \quad (3)$$

where A is the value in the absorption spectrum at the same concentration used to measure the CD spectrum. Obviously, the *g*-factor is independent of nanocrystal concentration in solution.

Data availability

The data are available from the corresponding authors on reasonable request.

References

26. Zhuang, T. T. et al. Controlled synthesis of kinked ultrathin ZnS nanorods/nanowires triggered by chloride ions: a case study. *Small* **10**, 1394–1402 (2014).
27. Schellman, J. A. Circular dichroism and optical rotation. *Chem. Rev.* **75**, 323–331 (1975).
28. Han, B., Zhu, Z., Li, Z., Zhang, W. & Tang, Z. Conformation modulated optical activity enhancement in chiral cysteine and Au nanorod assemblies. *J. Am. Chem. Soc.* **136**, 16104–16107 (2014).

Acknowledgements

This work was supported by the National Natural Science Foundation of China (grant nos. 51732011, 21431006, 21761132008, 81788101, 11227901 and 21805188), the Foundation for Innovative Research Groups of the National Natural Science Foundation of China (grant no. 21521001), Key Research Programme of Frontier Sciences, CAS (grant no. QYZDJ-SSW-SLH036), the National Basic Research Programme of China (grant no. 2014CB931800), the Users with Excellence and Scientific Research Grant of Hefei Science Centre of CAS (grant no. 2015HSC-UE007), Anhui Initiative in Quantum Information Technologies (grant no. AHY050000), Ontario Research Fund–Research Excellence Program and the Natural Sciences and Engineering Research Council of Canada.

Author contributions

S.-H.Y., E.H.S. and Z.T. supervised the project. T.-T.Z. and Y.Li conceived the idea, carried out the experiments, analysed the results and wrote the paper. X.G. helped to perform and analyse the circular dichroism and magnetic circular dichroism data. M.W. and Y.Li collected and analysed the transient absorption spectra. C.Z. helped to synthesize materials. L.D. and Y.-H.S. helped to conduct the magnetothermal and photothermal experiments. J.T. and G.L. helped to characterize the materials. F.P.G.d.A., P.T., X.L., Y.Lu, X.Y., L.Z., F.F. and S.O.K. helped to edit the manuscript. All authors discussed the results and assisted during manuscript preparation.

Competing interests

The authors declare no competing interests.

Additional information

Supplementary information is available for this paper at https://doi.org/10.1038/s41565-019-0606-8.

Correspondence and requests for materials should be addressed to S.-H.Y., Z.T. or E.H.S.

Peer review information *Nature Nanotechnology* thanks Hua Zhang and the other, anonymous, reviewer(s) for their contribution to the peer review of this work.

Reprints and permissions information is available at www.nature.com/reprints.